Ptychographic X-ray computed tomography at a high-brilliance X-ray source

SIMONE SALA,[1,2,3,*] DARREN J. BATEY,[2] ANUPAMA PRAKASH,[4] SHARIF AHMED,[2] CHRISTOPH RAU,[2] AND PIERRE THIBAULT[3]

[1]*Department of Physics and Astronomy, University College London, London WC1E 6BT, UK*
[2]*Diamond Light Source, Harwell Science and Innovation Campus, Didcot OX11 0DE, UK*
[3]*Department of Physics and Astronomy, University of Southampton, Southampton SO17 1BJ, UK*
[4]*Department of Biological Sciences, National University of Singapore, Singapore 117543*
[*]*simone.sala.14@ucl.ac.uk*

Abstract: Ptychographic X-ray computed tomography is a phase-contrast imaging technique capable of retrieving three-dimensional maps of the index of refraction of the imaged volumes with nanometric resolution. Despite its unmatched reach, its application remains prerogative of a limited number of laboratories at synchrotron sources. We present a detailed description of an experimental procedure and a data analysis pipeline which can be both exploited for ptychographic X-ray computed tomography experiments at any high-brilliance X-ray source. These have been validated at the I13-1 Coherence Branchline within the first experiment of its kind to be successfully carried out on a biological sample at Diamond Light Source.

1. Introduction

The first experimental demonstration of a technique which evolved into modern X-ray ptychography occurred just over two decades ago [1, 2]. The development and implementation of iterative phase retrieval algorithms [3–5] was soon accelerated by the introduction of fast and efficient algorithms [6, 7] which made X-ray ptychography a widely applicable phase-contrast imaging technique, capable of retrieving complex-valued maps of the index of refraction of extended areas [8]. Since then, X-ray ptychography has been implemented and is routinely used at several high-coherence experimental end stations at synchrotron sources worldwide [9–15]. At first limited to returning two-dimensional (2D) projections of the imaged areas, X-ray ptychography was soon demonstrated to be compatible with computed tomography (CT) and hence able to provide three-dimensional (3D) quantitative characterisation of scattering specimens. The first implementation of ptychographic X-ray computed tomography (PXCT) occurred at the cSAXS beamline at the Swiss Light Source [16], which kept leading the development of such kind of ptychography experiments [17–21]. However, PXCT remains more technically challenging than other 2D ptychography experiments on account of both experimental constraints and the relatively higher complexity of the data analysis pipeline. This is reflected in the fact that – unlike 2D ptychography – PXCT saw limited and delayed application outside cSAXS [22–25].

Despite the challenges it poses, PXCT still is of great appeal for the X-ray microscopy community as a technique to obtain high-resolution phase-contrast reconstructions of volumes, hardly achievable through any other X-ray method. This motivated the investment into developing it at other beamlines, in order to make it available to the wider non-specialist user community.

In this paper, we present the first successful demonstration of PXCT on a biogenic sample, of interest for a biology research group, at Diamond Light Source (DLS). The experiment was carried out at the I13-1 Coherence Branchline [26] which features ptychography [27, 28] and PXCT [29, 30] among its subjects of research. The procedure for data acquisition and analysis is compatible with and hence applicable to other high-brilliance X-ray sources.

2. Sample

A non-destructive PXCT experiment was carried out on a scale extracted from the wing of a pansy butterfly (*Junonia orithya*), aimed at characterising its 3D morphology. Individual scales are products of single cells [31] which develop on butterfly wings during the pupal stage, with each scale producing only one colour. Their basic structure is built out of chitin [$(C_8H_{13}O_5N)_n$] and consists of a thin lower lamina and an intricately patterned upper lamina, connected to each other via pillar-like trabeculae. The patterned upper lamina is made of longitudinal ridges interconnected by crossribs, creating open spaces called windows [32] [cf Fig. 1]. Colours are produced either by modifications to the basic scale structure, which can lead to structural colours via visible light interference effects [32], or by the deposition of pigments in the chitin matrix. Understanding the development of these scale morphologies and how small structural differences can affect colouration is currently of interest from both a developmental and bioengineering aspect.

Figure 1(a) shows a 20X magnification, transmitted light optical micrograph of the butterfly wing scale used as sample, which was glued on top of a 70 μm kapton MicroLoop and mounted on a sample holder. The image reveals the scale's longitudinal ridges. Both Bragg and coherent X-ray diffraction experiments have been previously run on other butterfly scales with the purpose of characterising the photonic nanostructures they contain [33]. That concept is here explored further by running a PXCT experiment aimed at the volumetric characterisation of a single butterfly wing scale.

Considering the thickest structures hosted in the chitin scale are known to span around 1 μm, an estimate can be generated of the magnitude of the absorption and phase-shift that radiation undergoes when travelling along the shortest path through the sample. Such path is achieved at the sample's widest orientation, i.e. the orientation at which the sample's main plane lies perpendicular to the optical axis. The index of refraction of a medium for radiation of energy E and wavelength λ can be defined as $n = 1 - \delta + i\beta$ with $\delta(E, \lambda)$ and $\beta(E, \lambda)$ as medium-dependent real functions. The PXCT experiment discussed in this paper was carried out at 9.7 keV – equivalent to a wavelength of 1.3 Å. At this energy, chitin has values for δ and β of 3.2×10^{-6} and 5.4×10^{-9}, respectively. The multiplicative complex-valued transmission function of the thin sample can be defined as

$$O(x, y, z) = e^{ik \int [n(x,y,z)-1]dz} = e^{-k \int \beta(x,y,z)dz} e^{-ik \int \delta(x,y,z)dz} \tag{1}$$

with the wave vector $k = 2\pi/\lambda$ and with z as the optical axis. This implies that at the sample's widest orientation only 0.05% of the incident radiation is absorbed while the phase of the transmitted radiation is shifted by $\pi/20$. Therefore, the main source of contrast of this weakly-scattering sample is phase shift.

The need for phase-contrast images requires and justifies the use of ptychography, while the radiation resistance of chitin – higher relative to other biogenic tissues – reduces the risk for the sample to suffer radiation damage during the long exposure of a tomographic scan. For these reasons and considering PXCT has already been established elsewhere on test samples, butterfly wing scales are suitable for validating this technique for and on biological samples and at the same time gather useful information for application outside the domain of technique development.

3. Experimental setup and data acquisition

As phase-retrieval is practically achievable only when exploiting at least partially coherent radiation [34], a high degree of coherence is typically made available at beamlines dedicated to ptychography experiments. Longitudinal coherence ξ_l with respect to the optical axis depends on bandwidth and is ensured using monochromators. Transverse coherence ξ_t is more
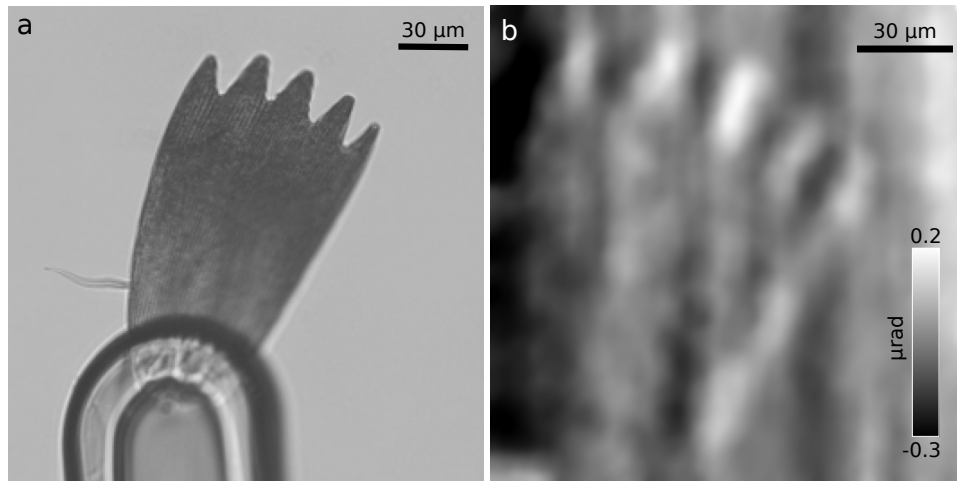
Fig. 1. (a) Transmitted light micrograph and (b) horizontal refraction image of a wing scale from a pansy butterfly mounted on holder.
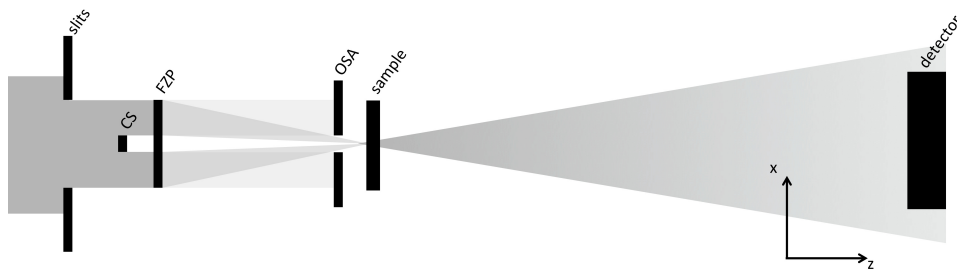

Fig. 2. Horizontal section of ptychographic X-ray computed tomography (PXCT) experimental setup including beam-shaping slits, central stop (CS), Fresnel focusing zone plate (FZP), order sorting aperture (OSA), translation and rotation sample stages (sample) and detector.

geometry-dependent and can be defined as

$$\xi_t = \frac{1}{2}\frac{\lambda R}{D} \tag{2}$$

with λ as the wavelength of the X-ray beam, R as the distance from the source and D as the distance between point sources which corresponds to the characteristic size of the source. One can further distinguish between vertical and horizontal coherence lengths which differ for most experiments. It can be noted that there exist two ways to increase ξ_t. One way is to reduce the source size and hence D and is achieved by reducing the gap of beam-shaping adjustable slits located at the front-end [cf Fig. 2], i.e. as close as possible to the already naturally small undulator source. The slits effectively produce a secondary source of tunable size and this approach is in place at several beamlines. The second way is to increase the distance R from the source which brought to the design of long beamlines, able to provide a high flux of highly coherent X-rays suitable for coherent imaging experiments preserving phase information.

The PXCT experiment described in this paper was carried out at the I13-1 Coherence Branchline [26] at DLS. This is a long coherent beamline and has its experimental hutch in a satellite building located outside the main building hosting the storage ring and its undulator source, making it some 250 m long in total. Figure 2 is a diagram of an experimental setup

suited for PXCT experiments and it was exploited for this one. Beam-shaping adjustable slits were used to tune the secondary source size and thus optimise the balance between photon flux and transverse coherence. A 9.7 keV X-ray beam was obtained through the beamline pseudo-channel-cut crystals Si monochromator. The beam was focussed using a Fresnel focusing zone plate (FZP) with a diameter of 400 μm and an outermost zone width of 150 nm in combination with a central stop (CS) with a diameter of 40 μm and an order sorting aperture (OSA) with a diameter of 10 μm. The sample holder was mounted on both a 3-axis translation and a 3-axis rotation stages located some 15 mm downstream from the focal position in order to exploit a divergent beam with a diameter of 13 μm. The rotation stage provided 360° rotation around the y axis which fulfils the general requirement of tomography for a 180° rotation around an axis perpendicular to the optical axis z to be carried out. A far-field geometry was used and the detector EXCALIBUR was positioned 14.6 m downstream from the sample, well into the far-field propagation regime. EXCALIBUR is the 2069×1796-pixel photon-counting beamline detector, based on Medipix3 chips with 55 μm pixel size [35]. A He-filled flight tube was positioned between the sample and the detector in order to minimise absorption and scattering from air.

Optics alignment was carried out which consisted of aligning all optical elements involved, namely the X-ray beam with respect to the adjustable slits, the monochromator, the focusing optics (CS, FZP, OSA), the sample stage and its rotation axis, the flight tube and the detector. Routine beam characterisation checks followed, exploiting a Siemens star test pattern in order to retrieve the wavefront at the sample position both to validate geometry and probe size and to obtain a robust initial guess for the probe for later reconstructions. The outcome of this procedure is visible in Figs. 3(a) and 3(b) which show the phase image of the Siemens star and the dominant mode of the illumination impinging on it, respectively. They were both retrieved through ptychographic reconstruction, as discussed in more details in the next section. Only limited decoherence effects were found thanks to the high degree of coherence available at the beamline, ensured also by operating with a relatively tight horizontal opening of 100 μm for the front-end slit. In fact, the main coherent mode of Fig. 3(b) accounts for 96.5% of the overall power of the retrieved probe.

After testing the experimental setup with the Siemens star, finer alignment was carried out on
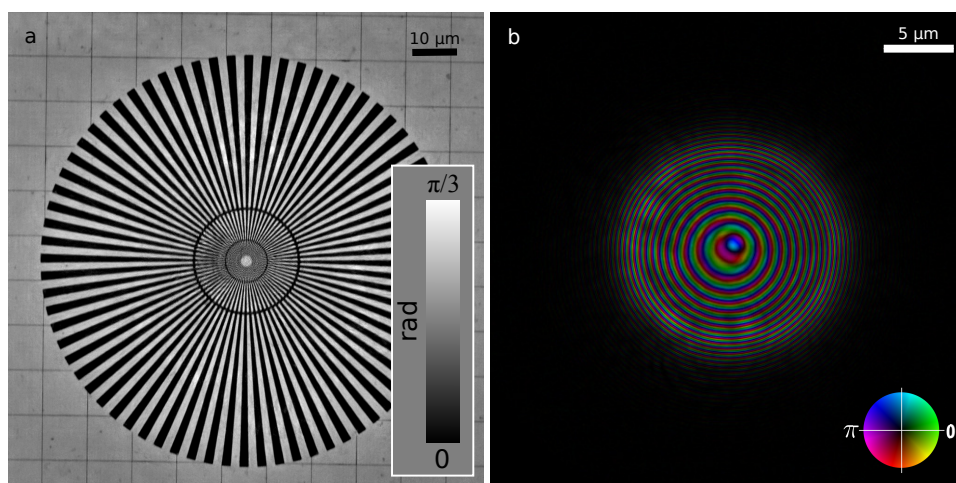

Fig. 3. (a) Phase part of the object and (b) complex-valued wavefront of the dominant mode (96.5% of total power) of the probe, both obtained from a ptychographic reconstruction run on a Siemens star test pattern. In (b) amplitude is mapped to brightness and phase to hue according to the colour wheel.

the butterfly wing scale, with particular care for aligning the area to be imaged in 3D with the rotation axis, which is a standard procedure whenever setting up tomographic experiments.

Scanning transmission X-ray microscopy (STXM) scans were performed to produce low-resolution overview images of the whole sample and specific regions of interest. The use of STXM to confirm sample position and orientation is a standard procedure within ptychography experiments on extended samples [36]. An example of such low-resolution STXM overviews is shown in Fig. 1(b) as the horizontal refraction image of the whole scale, obtained from differential phase-contrast STXM data.

The PXCT dataset was collected by performing 6 interlaced series of ptychography scans in order to minimise risks from time limitation and potential failure of any setup component. Considering the angle around the rotation axis of the rotation stage parallel to the y axis, each series was made up of 224 scans within the angular range 0-180° with an increment of 0.8° for a total of 1344 scans. Each scan was collected in move-settle-measure mode exploiting a 10×9-point snake scan, i.e. a row-by-row raster scan, inverting the order of the horizontal points at every row to reduce motor overhead. A step size of 4 μm was used to ensure a large amount of overlap among adjacent positions, leading to the illumination of an overall area over 50×50 μm^2 wide featuring between 1 and 4 of the tips of the jagged apical region of the wing scale as visible in Fig. 4. Finally, an exposure time of 0.9 s was selected to compromise between a high signal-to-noise ratio for each diffraction pattern and a short scanning time, leading to an overall scan duration of 55 h, inclusive of pauses for optics realignment to correct for long-term drifts. No radiation damage was observed throughout such long exposure which delivered a maximum dose estimated at 60 kGy, confirming the dose resistance of this biogenic sample.

4. Data analysis

Ptychographic reconstruction was run on each scan in order to retrieve 2D projections at every angle of the tomographic dataset and following the ptychographic pipeline schematically represented in Fig. 5. A mixed-state approach [34] was used with a 2-mode probe using the probe retrieved from the test pattern as an initial guess [cf Fig. 3(b)]. Each diffraction pattern – recorded directly in units of number of photons – was cropped down to a size of 512×512 pixels which, combined with the chosen geometry, led to a reconstruction pixel size of 66.3 nm.

Some ptychographic reconstruction algorithms are available [7, 37]: for this study, the mixed-
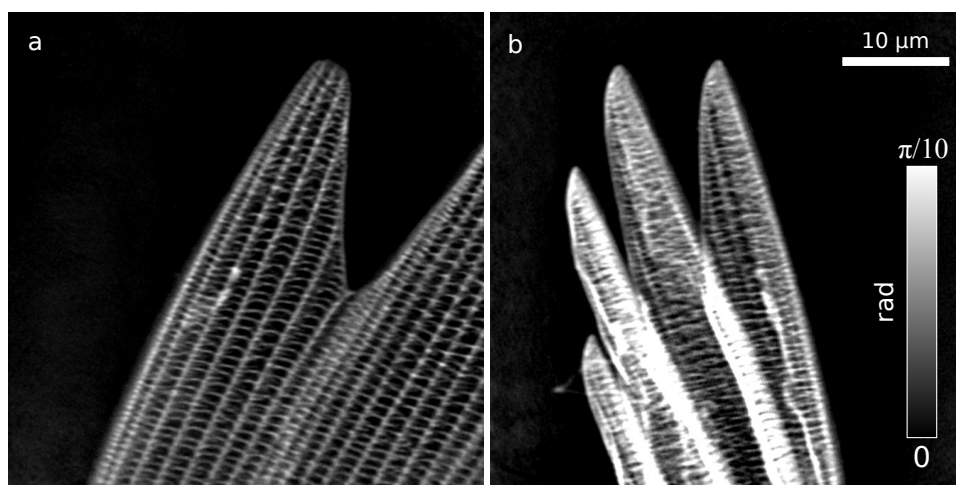

Fig. 4. Phase images of the apical region of a wing scale from a pansy butterfly collected at different sample orientations: (a) 0° and (b) 146°.

state approach available within the Python-based package *PtyPy* [38] was used, with 1000 iterations of difference map (DM) algorithm [6] followed by another 1000 iterations of maximum likelihood (ML) refinement [39]. Exploiting parallel computing on 16 CPUs, each projection took around 70 minutes to reconstruct. Larger detector frames and a higher number of probe modes would lead to larger compute-times while GPU-based algorithms would reduce it. In this case, the use of a shared compute cluster with 750 16-CPU compute nodes allowed to run all reconstructions within a few days, depending on queuing time.

A standard post-processing routine was performed on each reconstructed object in order to obtain a meaningful representation of the phase shift induced by the probe-object interaction [17]. As a first step, a linear and a constant phase terms were removed from each projection, equivalent to removing a phase ramp and a phase offset, respectively. This was achieved exploiting areas of each projection falling outside the sample, i.e. areas for which X-rays travelled through air, without undergoing any significant phase shift. For this purpose, projection-specific masks were generated by thresholding the phase part of each reconstructed object after applying first-order gaussian smoothing filters. After correcting for offset and linear ramp, phase unwrapping was carried out to obtain a continuous scale for the phase shift. This led to results such those from Fig. 4 which shows the phase images of the scale for two different projections, i.e. at two different sample orientations. Only the phase part of each reconstruction was deemed reliable due to the very low absorption of such thin sample. The retrieved phases confirm the success of the ptychographic reconstruction as weakly-scattering nanometric features are resolved, such as longitudinal ridges and crossribs.

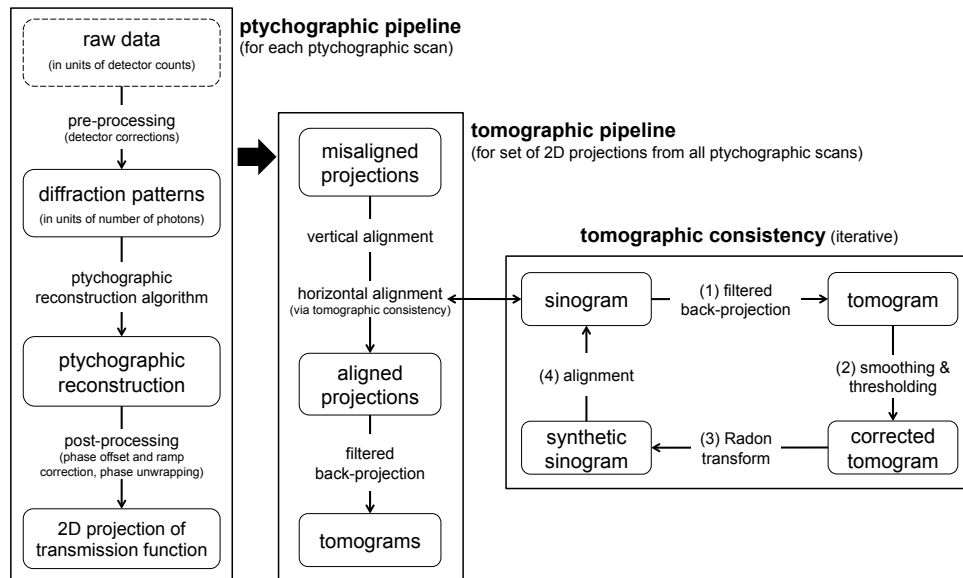Once all 2D phase projections were retrieved and corrected, they became a dataset suitable for

Fig. 5. Schematic representation of PXCT data analysis pipeline. The ptychographic pipeline is aimed at obtaining 2D projections of the transmission function of the imaged object, starting from the raw data recorded by the detector for each ptychographic scan. The tomographic pipeline is aimed at obtaining a stack of 2D tomograms (i.e. a whole volume) starting from the whole set of 2D projections obtained from the ptychographic pipeline. Tomographic consistency is the iterative algorithm exploited for horizontal alignment of the partial local tomography data set.

tomographic analysis. This was undertaken following the tomographic pipeline schematically represented in Fig. 5. In order to produce sinograms suited for filtered back-projection (FBP), individual 2D projections had to be aligned with respect to each other, both vertically and horizontally. Some basic alignment procedure for ptychographic projections within tomographic experiments has already been proposed [17]. The fact that for these measurements parts of the imaged samples fell out of the field-of-view at several orientations, however, required a more elaborate aligning procedure, especially suited to tackle issues of missing wedge or – as it was the case for these reconstructions – partial local tomography. In particular, a customised implementation of the tomographic consistency approach [40] was found successful.

First, vertical alignment was carried out exploiting a first-order – vertical derivative only – gaussian smoothing filter able to highlight the top pixel of the sample at every orientation by comparing the maximum values of each row. Cross-correlation was then applied to this collection of values for the topmost area of each projection to vertically align them within pixel precision.

For horizontal alignment, an iterative approach inspired by the principle of tomographic consistency was applied, as schematically represented in Fig. 5. A sinogram was produced as the mean of a series of sinograms within a narrow vertical range (10 pixels). Such mean sinogram was then padded, both to compensate for misalignment of the rotation axis with respect to the centre of the field-of-view of the reconstructions and to expand the field-of-view itself enough to include at least the second tip of the scale, visible only at about 2/3 of the collected sample orientations [cf Fig. 4]. At each iteration, a filtered back-projection was applied to the sinogram exploiting a Hamming window and an inverse Radon transform and generating a tomogram (step 1). A smoothing filter and some lower- and upper-value thresholding were applied to such tomogram (step 2) which was then projected back to the sinogram space via Radon transformation (step 3), generating a naturally-aligned synthetic sinogram within the whole padded field-of-view. This was used as a reference to align the original projections contained within the sinogram from the previous iteration – i.e. before step 1 – via a windowed cross-correlation (step 4), concluding a full 4-step iteration. A few such iterations (3-6) were already enough to achieve horizontal alignment within pixel precision, allowing for tomographic reconstruction to be run on the full dataset.
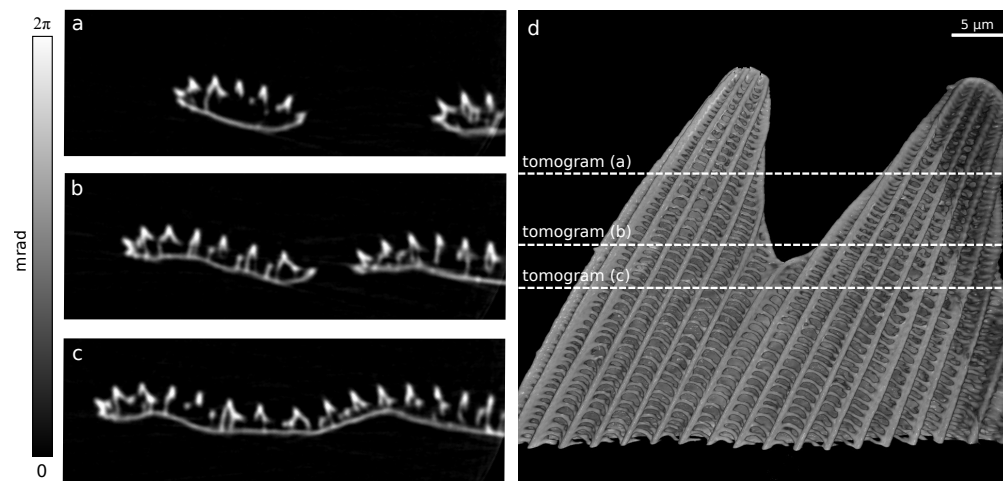

Fig. 6. (a-c) Phase tomograms at different heights, including two tips of the apical region of a wing scale from a pansy butterfly. (d) 3D rendering obtained from a stack of 750 such phase tomograms using Drishti [41]. Regions to which tomograms from (a), (b) and (c) refer are annotated in (d).

Applying FBP to the corrected phase part of the full stack of aligned projections led to the results shown in Fig. 6. In particular Figs. 6(a)-6(c) show phase tomograms of a region including 2 scale tips while Fig. 6(d) shows a 3D-rendered image of the whole reconstructed phase volume, obtained exploiting the open-source volume exploration package Drishti [41]. From cuts through sharp edges in Figs. 6(a)-6(c), the achieved resolution was estimated at 250 nm. In Fig. 6(d), the reconstruction of part of the second scale tip (right-hand side) results of lower quality: this is due to the fact that such region – along with others beyond it – was not imaged in all 2D projections, leading to artefacts.

Both tomograms and 3D rendering reveal the nanostructures of the butterfly wing scale. Lower lamina, longitudinal ridges and crossribs are all clearly visible. Furthermore, the use of rendering tools allows to explore the trabecular structures connecting lower and upper laminae and characterise the windows, i.e. the open spaces between them, which would hardly be accessible through 2D microscopy techniques.

Unlike ptychographic reconstruction, the rest of the data analysis – post-processing, projection alignment and FBP – was not highly compute-intensive, to the point it did not need parallelisation. On the other hand, it required a high degree of customisation which ended up taking several days. It is expected future experiments will benefit from the developed data processing pipeline which will lead to reaching final results faster.

5. Summary and conclusions

We presented the first successful PXCT experiment carried out on a biogenic sample at Diamond Light Source (DLS). In particular, the experiment involved a weakly-scattering butterfly wing scale hosting chitin nanostructures of interest – among others – for a research group focusing on evolutionary developmental biology. Ptychographic analysis produced a full set of phase-contrast 2D projections at several sample orientations. Tomographic analysis on this set produced a quantitative volumetric reconstruction of the scanned region which – in particular exploiting 3D rendering and exploration tools – can be investigated for structure determination and comparison at high resolution. In that sense, this study demonstrates the viability of PXCT as a high-resolution imaging method for reproducible and non-destructive analysis of butterfly wing scales from different individuals and species. This makes PXCT a great tool to visualise and understand the mechanisms of biophotonic structure development and to characterise gene-driven structural differences at high resolution.

In general, the success of PXCT within this experiment also contributes to the advancement of one more X-ray imaging tool, able to retrieve phase-contrast high-resolution volumetric reconstructions. This step forward is expected to benefit the wider X-ray microscopy community.

Finally, the data acquisition and analysis pipeline presented in this paper is reproducible at other high-brilliance X-ray sources, making PXCT more readily accessible by providing a step-by-step guide on how to carry out such experiments and efficiently handle the high-resolution data they produce.

References

1. H. N. Chapman, "Phase-retrieval X-ray microscopy by Wigner-distribution deconvolution," Ultramicroscopy **66**, 153–172 (1996).
2. H. N. Chapman, "Phase-retrieval X-ray microscopy by Wigner-distribution deconvolution: signal processing," Scanning Microsc. **11**, 67–80 (1997).
3. H. M. L. Faulkner and J. M. Rodenburg, "Movable aperture lensless transmission microscopy: a novel phase retrieval algorithm," Phys. Rev. Lett. **93**, 023903 (2004).
4. J. M. Rodenburg and H. M. L. Faulkner, "A phase retrieval algorithm for shifting illumination," Appl. Phys. Lett. **85**, 4795–4797 (2004).
5. J. M. Rodenburg, A. C. Hurst, A. G. Cullis, B. R. Dobson, F. Pfeiffer, O. Bunk, C. David, K. Jefimovs, and I. Johnson, "Hard-X-ray lensless imaging of extended objects," Phys. Rev. Lett. **98**, 1–4 (2007).
6. P. Thibault, M. Dierolf, O. Bunk, A. Menzel, and F. Pfeiffer, "Probe retrieval in ptychographic coherent diffractive imaging," Ultramicroscopy **109**, 338–343 (2009).
7. A. M. Maiden and J. M. Rodenburg, "An improved ptychographical phase retrieval algorithm for diffractive imaging," Ultramicroscopy **109**, 1256–1262 (2009).
8. F. Pfeiffer, "X-ray ptychography," Nat. Photonics **12**, 9–17 (2018).
9. Y. Takahashi, A. Suzuki, N. Zettsu, Y. Kohmura, Y. Senba, H. Ohashi, K. Yamauchi, and T. Ishikawa, "Towards high-resolution ptychographic x-ray diffraction microscopy," Phys. Rev. B **83**, 1–5 (2011).
10. M. Beckers, T. Senkbeil, T. Gorniak, M. Reese, K. Giewekemeyer, S. C. Gleber, T. Salditt, and A. Rosenhahn, "Chemical contrast in soft X-ray ptychography," Phys. Rev. Lett. **107**, 1–4 (2011).
11. A. Schropp, R. Hoppe, J. Patommel, D. Samberg, F. Seiboth, S. Stephan, G. Wellenreuther, G. Falkenberg, and C. G. Schroer, "Hard x-ray scanning microscopy with coherent radiation: Beyond the resolution of conventional x-ray microscopes," Appl. Phys. Lett. **100**, 10–13 (2012).
12. A. M. Maiden, G. R. Morrison, B. Kaulich, A. Gianoncelli, and J. M. Rodenburg, "Soft X-ray spectromicroscopy using ptychography with randomly phased illumination," Nat. Commun. **4**, 1666–1669 (2013).
13. D. A. Shapiro, Y. S. Yu, T. Tyliszczak, J. Cabana, R. Celestre, W. Chao, K. Kaznatcheev, A. L. Kilcoyne, F. Maia, S. Marchesini, Y. S. Meng, T. Warwick, L. L. Yang, and H. A. Padmore, "Chemical composition mapping with nanometre resolution by soft X-ray microscopy," Nat. Photonics **8**, 765–769 (2014).
14. J. C. da Silva, A. Pacureanu, Y. Yang, F. Fus, M. Hubert, L. Bloch, M. Salome, S. Bohic, and P. Cloetens, "High-energy cryo x-ray nano-imaging at the ID16A beamline of ESRF," Proc. SPIE **10389**, 103890F (2017).
15. U. Vogt, K. Parfeniukas, T. Stankevic, S. Kalbfleisch, Z. Matej, A. Björling, M. Liebi, G. Carbone, A. Mikkelsen, and U. Johansson, "First x-ray nanoimaging experiments at NanoMAX," Proc. SPIE **10389**, 103890K (2017).
16. M. Dierolf, A. Menzel, P. Thibault, P. Schneider, C. M. Kewish, R. Wepf, O. Bunk, and F. Pfeiffer, "Ptychographic X-ray computed tomography at the nanoscale." Nature **467**, 436–439 (2010).
17. M. Guizar-Sicairos, A. Diaz, M. Holler, M. S. Lucas, A. Menzel, R. a. Wepf, and O. Bunk, "Phase tomography from x-ray coherent diffractive imaging projections," Opt. Express **19**, 21345–21357 (2011).
18. A. Diaz, P. Trtik, M. Guizar-Sicairos, A. Menzel, P. Thibault, and O. Bunk, "Quantitative x-ray phase nanotomography," Phys. Rev. B **85**, 1–4 (2012).
19. M. Holler, A. Diaz, M. Guizar-Sicairos, P. Karvinen, E. Färm, E. Härkönen, M. Ritala, A. Menzel, J. Raabe, and O. Bunk, "X-ray ptychographic computed tomography at 16 nm isotropic 3D resolution." Sci. Rep. **4**, 1–5 (2014).
20. M. Guizar-Sicairos, M. Holler, A. Diaz, J. C. da Silva, E. H. R. Tsai, O. Bunk, C. Martinez-Perez, P. C. J. Donoghue, C. H. Wellman, and A. Menzel, "Ptychographic nanotomography at the Swiss Light Source," Proc. SPIE **9592**, 95920A (2015).
21. M. Holler, M. Guizar-Sicairos, E. H. Tsai, R. Dinapoli, E. Müller, O. Bunk, J. Raabe, and G. Aeppli, "High-resolution non-destructive three-dimensional imaging of integrated circuits," Nature **543**, 402–406 (2017).
22. M. Stockmar, M. Hubert, M. Dierolf, B. Enders, R. Clare, S. Allner, A. Fehringer, I. Zanette, J. Villanova, J. Laurencin, P. Cloetens, F. Pfeiffer, and P. Thibault, "X-ray nanotomography using near-field ptychography," Opt. Express **23**, 12720–12731 (2015).
23. J. C. da Silva, J. Haubrich, G. Requena, M. Hubert, A. Pacureanu, L. Bloch, Y. Yang, and P. Cloetens, "High energy near- and far-field ptychographic tomography at the ESRF," Proc. SPIE **10391**, 1039106 (2017).
24. Y. S. Yu, M. Farmand, C. Kim, Y. Liu, C. P. Grey, F. C. Strobridge, T. Tyliszczak, R. Celestre, P. Denes, J. Joseph, H. Krishnan, F. R. Maia, A. L. Kilcoyne, S. Marchesini, T. P. C. Leite, T. Warwick, H. Padmore, J. Cabana, and D. A. Shapiro, "Three-dimensional localization of nanoscale battery reactions using soft X-ray tomography," Nat. Commun. **9**, 1–7 (2018).
25. M. Kahnt, G. Falkenberg, J. Garrevoet, J. Hartmann, T. Krause, M. Niehle, M. Scholz, M. Seyrich, A. Trampert, A. Waag, H.-H. Wehmann, F. Wittwer, H. Zhou, M. Hanke, and C. G. Schroer, "Simultaneous hard X-ray ptychographic tomography and X-ray fluorescence tomography of isolated hollow core-shell GaN rods," Microsc. Microanal. **24**, 34–35 (2018).

26. C. Rau, U. Wagner, Z. Pešić, and A. De Fanis, "Coherent imaging at the Diamond beamline I13," Phys. Status Solidi A **208**, 2522–2525 (2011).

27. T. B. Edo, D. J. Batey, A. M. Maiden, C. Rau, U. Wagner, Z. D. Pešić, T. A. Waigh, and J. M. Rodenburg, "Sampling in x-ray ptychography," Phys. Rev. A **87**, 1–8 (2013).

28. D. J. Batey, T. B. Edo, C. Rau, U. Wagner, Z. D. Pešić, T. A. Waigh, and J. M. Rodenburg, "Reciprocal-space up-sampling from real-space oversampling in x-ray ptychography," Phys. Rev. A **89**, 1–5 (2014).

29. P. Li, "Investigations and improvements in ptychographic imaging," Phd thesis, University of Sheffield (2016).

30. D. Batey, S. Cipiccia, X. Shi, S. Williams, K. Wanelik, A. Wilson, S. Pérez-Tamarit, P. Cimavilla, M. A. Ródriguez-Pérez, and C. Rau, "Coherence Branch at I13, DLS: The Multiscale, Multimodal, Ptycho-tomographic End Station," Microsc. Microanal. **24**, 42–43 (2018).

31. H. Ghiradella, "Structure of butterfly scales: patterning in an insect cuticle," Microsc. Res. Tech. **27**, 429–438 (1994).

32. H. Ghiradella, "Insect cuticular surface modifications: scales and other structural formations," in *Advances in Insect Physiology,* J. Casas and S. J. Simpson, eds. (Elsevier Ltd, 2010), chap. 4, pp. 135–180.

33. A. Singer, L. Boucheron, S. H. Dietze, K. E. Jensen, D. Vine, I. McNulty, E. R. Dufresne, R. O. Prum, S. G. J. Mochrie, and O. G. Shpyrko, "Domain morphology, boundaries, and topological defects in biophotonic gyroid nanostructures of butterfly wing scales," Sci. Adv. **2**, e1600149 (2016).

34. P. Thibault and A. Menzel, "Reconstructing state mixtures from diffraction measurements supplement," Nature **494**, 68–71 (2013).

35. J. Marchal, I. Horswell, B. Willis, R. Plackett, E. N. Gimenez, J. Spiers, D. Ballard, P. Booker, J. A. Thompson, P. Gibbons, S. R. Burge, T. Nicholls, J. Lipp, and N. Tartoni, "EXCALIBUR: a small-pixel photon counting area detector for coherent X-ray diffraction - front-end design, fabrication and characterisation," J. Phys. Conf. Ser. **425**, 062003 (2013).

36. S. Sala, V. S. C. Kuppili, S. Chalkidis, D. J. Batey, X. Shi, C. Rau, and P. Thibault, "Multiscale X-ray imaging using ptychography," J. Synchrotron Radiat. **25**, 1214–1221 (2018).

37. S. Marchesini, H. Krishnan, B. J. Daurer, D. A. Shapiro, T. Perciano, J. A. Sethian, and F. R. N. C. Maia, "SHARP: a distributed GPU-based ptychographic solver," J. Appl. Crystallogr. **49**, 1245–1252 (2016).

38. B. Enders and P. Thibault, "A computational framework for ptychographic reconstructions," Proc. R. Soc. A **472**, 1–19 (2016).

39. P. Thibault and M. Guizar-Sicairos, "Maximum-likelihood refinement for coherent diffractive imaging," New J. Phys. **14**, 063004 (2012).

40. M. Guizar-Sicairos, J. J. Boon, K. Mader, A. Diaz, A. Menzel, and O. Bunk, "Quantitative interior x-ray nanotomography by a hybrid imaging technique," Optica **2**, 259–266 (2015).

41. A. Limaye, "Drishti: a volume exploration and presentation tool," Proc. SPIE **8506**, 85060X (2012).